1 **Quantifying the tropospheric ozone radiative effect and its temporal evolution in the satellite-era**

2 Richard J. Pope[1,2], Alexandru Rap[1], Matilda A. Pimlott[1], Brice Barret[3], Eric Le Flochmoen[3], Brian J.
3 Kerridge[4,5], Richard Siddans[4,5], Barry G. Latter[4,5], Lucy J. Ventress[4,5], Anne Boynard[6,7], Christian
4 Retscher[8], Wuhu Feng[1,9], Richard Rigby[1,10], Sandip S. Dhomse[1,2], Catherine Wespes[11] and Martyn P.
5 Chipperfield[1,2]

7 *1: School of Earth and Environment, University of Leeds, Leeds, UK*

8 *2: National Centre for Earth Observation, University of Leeds, Leeds, UK*

9 *3: LAERO/OMP, Université de Toulouse, Toulouse, France*

10 *4: Remote Sensing Group, STFC Rutherford Appleton Laboratory, Chilton, UK*

11 *5: National Centre for Earth Observation, STFC Rutherford Appleton Laboratory, Chilton, UK*

12 *6: LATMOS/IPSL, Sorbonne Université, UVSQ, CNRS, Paris, 75005, France*

13 *7: SPASCIA, Ramonville-Saint-Agne, 31520, France*

14 *8: ESA/ESRIN, Frascati, Italy*

15 *9: National Centre for Atmospheric Science, University of Leeds, Leeds, UK*

16 *10: Centre for Environmental Modelling and Computation, University of Leeds, Leeds, UK*

17 *11: Université libre de Bruxelles (ULB), Spectroscopy, Quantum Chemistry and Atmospheric Remote*
18 *Sensing, Brussels, Belgium*

19 Resubmitted to *Atmospheric Chemistry and Physics*

20 *Correspondence to*: Richard J. Pope (r.j.pope@leeds.ac.uk)

21 **Key Points:**

22 • Using satellite data and model simulations, we quantify the decadal (2008-2017) global
23 average tropospheric ozone radiative effect (TO$_3$RE) to range between 1.21 and 1.26 W/m^2.

24 • Satellite/modelled decadal (2008-2017) trends in the TO$_3$RE show negligible change with
25 time.

26 • This negligible trend in TO$_3$RE is caused by competing processes (meteorological variability
27 and temporal changes in precursor emissions) over the decade.

28 **Abstract:**

29 Using state-of-the-art satellite ozone profile products, and chemical transport model, we provide an
30 updated estimate of the tropospheric ozone radiative effect (TO$_3$RE) and observational constraint on
31 its variability over the decade 2008-2017. Previous studies have shown the short-term (i.e. a few
32 years) globally weighted average TO$_3$RE to be 1.17±0.03 W/m^2. However, from our analysis, using
33 decadal (2008-2017) ozone profile datasets from the Infrared Atmospheric Sounding Interferometer,
34 average TO$_3$RE ranges between 1.21 and 1.26 W/m^2. Over this decade, the modelled/observational
35 TO$_3$RE linear trends show negligible change (e.g. ±0.1%/year). Two model sensitivity experiments
36 fixing emissions and meteorology to one-year (i.e. start year – 2008) show that temporal changes in

37 ozone precursor emissions (increasing contribution) and meteorological factors (decreasing
38 contribution) have counteracting tendencies leading to a negligible globally weighted average TO_3RE
39 trend.

40 **Plain Language Summary:**

41 Tropospheric ozone is a potent air pollutant and an important short-lived climate forcer (SLCF). It is a
42 secondary pollutant formed through chemical reactions of precursor gases and sunlight. As a SLCF, it
43 influences both the incoming solar short-wave radiation and the outgoing long-wave radiation
44 throughout the troposphere but has the largest radiative impact in the upper troposphere where the
45 balance between the two yields a net positive (i.e. warming) effect at the surface. The majority of
46 previous estimates of the tropospheric ozone radiative effect (TO_3RE) have been quantified from
47 atmospheric chemistry climate model simulations. However, satellite retrievals of tropospheric
48 ozone now have decadal records and provide the opportunity to quantify the TO_3RE and
49 complement estimates based on model simulations. In this study, we utilise satellite ozone profile
50 retrievals from the Infrared Atmospheric Sounding Interferometer (IASI), on-board the MetOp-A
51 satellite, to derive a decadal average TO_3RE estimate of 1.21-1.26W/m^2. While this builds upon
52 previous studies (e.g. TO_3RE estimates of 1.17±0.03 W/m^2), the improved spatial coverage and
53 temporal record of IASI also allows for the assessment of TO_3RE variability and tendencies on a
54 decadal scale. Here, we find negligible trends in the TO_3RE (2008-2017) suggesting that the decadal
55 contribution of tropospheric ozone to climate, via radiative properties, has been limited.

1. Introduction

57 Tropospheric ozone (TO_3) is a short-lived climate forcer (SLCF; Forster et al., 2021; Szopa et al.,
58 2021). It is the third most important greenhouse gas (GHG; Forster et al., 2021; Myhre et al., 2013)
59 and a hazardous air pollutant with adverse impacts on human health (WHO, 2018; Fleming et al.,
60 2018) and the biosphere (e.g. agricultural and natural vegetation; Mills et al., 2018; Sitch et al.,
61 2007). Since the pre-industrial (PI) period, anthropogenic activities have increased the atmospheric
62 loading of ozone (O_3) precursor gases, most notably nitrogen oxides (NO_x) and methane (CH_4),
63 resulting in an increase in TO_3 of 25-50% since 1900 (Gauss et al., 2006; Lamarque et al., 2010; Szopa
64 et al., 2021; Young et al., 2013). More recently, since the mid-twentieth century, northern
65 hemispheric TO_3 has increased by 30-70%. The PI to present day (PD) radiative forcing (RF) from TO_3
66 is estimated by the Intergovernmental Panel on Climate Change (IPCC) to be 0.47 W m^{-2} (Forster et
67 al., 2021) with an uncertainty range of 0.24–0.70 W m^{-2}. While models provide a valuable framework
68 to quantify the TO_3 RF, observations are required to validate the models' representation of TO_3 and
69 TO_3 RF. Observations are not available for the PI, but multiple satellite products of TO_3 are readily
70 available in the PD (e.g. Richards et al., 2008; Boynard et al., 2018; Barret et al., 2020). The
71 tropospheric ozone radiative effect (TO_3RE) is defined as the radiative flux imbalance at the
72 tropopause between incoming short-wave solar radiation and the outgoing long-wave radiation due
73 to the presence of TO_3 (Rap et al., 2015). Therefore, satellite ozone profile datasets from infrared
74 instruments, in combination with off-line ozone radiative kernels (e.g. Bowman et al., 2013; Rap et
75 al., 2015), can be used to quantify the PD TO_3RE. This can then either constrain model estimates of
76 PD TO_3RE or be used directly with modelled PI TO_3RE to derive the TO_3RF.

77 Several studies have previously used satellite data to derive short-term estimates of the TO_3RE (i.e.
78 from a few months of data). Joiner et al., (2009) used tropospheric column ozone (TCO_3) data based
79 on two satellite instruments: Ozone Monitoring Instrument (OMI) and Microwave Limb Sounder

80 (MLS) measurements, also known as OMI-MLS product for January and July 2005, to estimate the
81 resultant instantaneous TO_3RE at the tropopause to be 1.53 W/m^2. Worden et al., (2008) used ozone
82 profile data for 2006 from the Tropospheric Emissions Spectrometer (TES), on-board NASA's Aura
83 satellite, to estimate the average instantaneous long-wave TO_3RE at the top-of-the-atmosphere
84 (TOA) over the oceans (45°S-45°N) to be 0.48±0.14 W/m^2. Worden et al., (2011), using TES data for
85 August 2006, estimated the instantaneous long-wave TO_3RE at TOA to be 0.33 W/m^2. Later, Bowman
86 et al., (2013) also used TES data (averaged between 2005 and 2009) to constrain the simulated
87 instantaneous long-wave TO_3RE from an ensemble model average. They found that seasonally, TES
88 long-wave TO_3RE peaks in northern Africa/Mediterranean/Middle East in June-July-August over 1.0
89 W/m^2 with minimum values (0.0-0.2 W/m^2) over the winter-time high-latitudes. Overall, the
90 ensemble average long-wave TO_3RE low bias was 0.12 W/m^2. Doniki et al., (2015) took this further
91 by calculating the instantaneous long-wave TO_3RE from the Infrared Atmospheric Sounding
92 Interferometer (IASI), though using a small subset of the data, and found estimates from Worden et
93 al., (2008), using TES, had a low bias of ~25%. Rap et al., (2015) also used TES satellite ozone profile
94 observations (2005-2008) in combination with the TOMCAT chemical transport model (CTM) and
95 provided the first robust satellite constraint on annual globally weighted resultant TO_3RE (after
96 stratospheric temperature adjustment) with a range of 1.17±0.03 W/m^2.

97 Following the methodology adopted in Rap et al. (2015), we exploit satellite ozone profile data from
98 IASI, on the MetOp-A satellite, which has a longer-term record and considerably denser spatial
99 coverage than TES, in combination with the TOMCAT CTM, to improve the TO_3RE estimate and
100 provide the first quantification of its decadal variability. The satellite data, radiation model and CTM
101 used are discussed in Section 2, our results are presented in Section 3 and Section 4 summarises our
102 conclusions.

103 **2. Observations and Model**

104 **2.1. Satellite Observations**

105 IASI is a Michelson interferometer with a nadir-viewing spectral range between 645 and 2760 cm^{-1}
106 with spectral sampling of 0.25 cm^{-1} (Illingworth et al., 2011). It measures simultaneously in four fields
107 of view (FOV, each circular at nadir with a diameter of 12 km) in a 50 x 50km square which are
108 scanned across track to sample a 2200 km-wide swath (Clerbaux et al., 2009). IASI, on Eumetsat's
109 MetOp-A satellite, is in a sun-synchronous polar orbit with equator crossing local times of 9.30 (day)
110 and 21.30 (night). Though, we only use IASI daytime data in this study.

111 The three IASI products we use in this study are the IASI-FORLI product (vn 20151001, IASI-FORLI,
112 2020; Boynard et al., 2018; Wespes et al., 2018), the IASI-SOFRID product (vn 3.5, IASI-SOFRID, 2022;
113 Barret et al., 2020) and the RAL IASI-IMS product (IASI-IMS, 2022; Pope et al., 2021; Pimlott et al.
114 ,2022) between 2008 and 2017 (i.e. period of consistent data coverage for all the IASI products). All
115 three products use an optimal estimation method (OEM, Rogers, 2000) to retrieve ozone. Both IASI-
116 SOFRID and IASI-IMS use the RTTOV radiative transfer model (Saunders et al. 1999), while the IASI-
117 FORLI product uses look-up tables to speed up its radiative transfer calculations (Hurtmans et al.,
118 2012). Meteorological inputs (pressure, water vapour, temperature and clouds) for IASI-FORLI come
119 from Eumetsat level-2 data, while IASI-SOFRID uses ECMWF operational analyses and IASI-IMS uses
120 ECMWF surface pressures and co-retrieves other meteorological and surface variables. For the
121 ozone apriori, IASI-FORLI and IASI-IMS use the ozone climatology of McPeters et al., (2007), while
122 IASI-SOFRID uses the dynamical ozone climatology described in Sofieva et al., (2014).

123 The IASI-FORLI level-2 data are filtered for a geometric cloud fraction <0.13, degrees of freedom >
124 2.0, O_3 values > 0.0, solar zenith angle < 80.0° and the surface to 450 hPa sub-column O_3 / total
125 column O_3 < 0.085. The IASI-SOFRID data were provided on a 1.0°×1.0° horizontal grid (i.e. level-3
126 product, but daily temporal resolution) with filtering already applied as in Barret et al., (2020). Here,
127 only O_3 values > 0.0 were used. For IASI-IMS level-2, the data are filtered for a geometric cloud
128 fraction <0.5, O_3 values > 0.0, solar zenith angle < 80.0° and a cost function < 1000.0. For IASI-IMS,
129 we relaxed the geometric cloud fraction threshold to 0.5 as it retains more data as the data product
130 in this study has only been processed for 1 in 10 days and 1 in 4 pixels.

131 Overall, IASI provides substantially denser spatial sampling and a longer-term record than its
132 predecessor instruments. For instance, TES provided homogenous global coverage, albeit with
133 sparse spatial sampling, every 16 days (Rap et al., 2013) over a 6-year period (2005-2010), while IASI
134 on MetOp-A provided comparatively dense global coverage twice per day between 2008 and 2020
135 (though we focus on 2008-20217 where the IASI products have consistent records). Thus, making it
136 suitable to investigate decadal average spatial patterns in TO_3RE and decadal scale interannual
137 variability.

2.2.   Ozonesondes

139 Despite the three IASI ozone profile products using the same radiance data, the three retrieval
140 schemes produced systematic differences between the products in the long-term TCO_3 average (e.g.
141 **Figures S2 and S3** from the **Supporting Information (SI)**). Though, the spatial structure in the three
142 products compares well. Therefore, to harmonise the three IASI TCO_3 data sets (i.e. absolute values
143 but not long-term variability) we use ozonesonde data from the World Ozone and Ultraviolet
144 Radiation Data Centre (WOUDC; WOUDC, 2023), the Southern Hemisphere ADditional Ozonesondes
145 (SHADOZ; SHADOZ, 2023) project and the Global Monitoring Laboratory, National Oceanic and
146 Atmospheric Administration (NOAA; NOAA, 2023). Here, O_3 measurements were rejected if the O_3 or
147 pressure values were unphysical (i.e. < 0.0), if the O_3 partial pressure > 2000.0 mPa or the O_3 value
148 was set to 99.9, and whole ozonesonde profiles were rejected if least 50% of the measurements did
149 not meet these criteria. These criteria are similar to those applied by Keppins et al., (2018) and
150 Hubert et al., (2016). To allow for direct like-for-like comparisons between the two quantities,
151 accounting for the vertical sensitivity of the satellite, the instrument averaging kernels (AKs) are
152 applied the ozonesonde profiles as:

$$sonde_{AK} = AK.(sonde_{int} - apr) + apr \qquad (1)$$

154 where $sonde_{AK}$ is the modified ozonesonde sub-column profile, AK is the averaging kernel matrix,
155 $sonde_{int}$ is the ozonesonde sub-column profile interpolated on the satellite pressure grid and apr is
156 the a priori for the satellite retrieval. For the application of the AKs to the ozonesonde profiles, the
157 full ozone profile is required which is not available from the ozonesondes (i.e. mid-stratosphere and
158 above). Therefore, the ozonesonde profile above its minimum pressure level is extended using the
159 apriori profile from the corresponding satellite product. The profile is smoothed vertically across the
160 joining pressure level to avoid a profile discontinuity.

161 Once the ozonesondes had been co-located with the satellite data (i.e. within 6-hours and 500 km)
162 and the AKs applied, the two datasets were compared across the full 2008-2017 period. We typically
163 find a global annual TCO_3 systematic bias of 14.9%, 2.7% and 17.4% for IASI-FORLI, IASI-SOFRID and
164 IASI-IMS, respectively, which is consistent with Boynard et al., (2018), Barret et al., (2020) and

165   Pimlott et al., (2022). Here, we generated annual-latitude (30° bins) bias correction factors (BCF)
166   which were applied to the gridded satellite records (**see SI-2**) to harmonise the retrieved TCO_3 (i.e.
167   remove the systematic errors) and scale the derived TO_3RE. This is an important exercise as it
168   provides a more accurate absolute range in satellite retrieved TCO_3 (and the ozone values used to
169   derive the TO_3RE) but as the ozonesondes generally have poor spatial coverage, the global coverage
170   and spatial distribution of the satellite data is critical in our analysis. Note, that as a climatology was
171   used, the systematic biases in the satellite records were affected but their long-term temporal
172   variability retained.

2.3. TOMCAT

174   In this study, we use the 3D global chemical transport model TOMCAT (Chipperfield, 2006), which
175   has a detailed tropospheric chemistry scheme including 229 gas-phase reactions and 82 advected
176   tracers (Monks et al., 2017). Model heterogeneous chemistry uses size-resolved aerosol from the
177   GLOMAP module (Mann et al., 2010). The model was run between 2008 and 2017 at a 2.8°×2.8°
178   spatial resolution with 31 vertical levels between the surface and 10hPa. Here, climatological fields
179   of trace gases/aerosols are used as the vertical boundary conditions (including stratospheric ozone).
180   The model is forced by meteorological reanalyses (ERA-Interim) from the European Centre for
181   Medium-Range Weather Forecasts (ECMWF; Dee et al., 2011) including reanalysis cloud fields and
182   mass fluxes (e.g. as in Rowlinson et al., 2020, Pimlott et al., 2022). Annually varying anthropogenic
183   emissions come from the Coupled Model Intercomparison Project Phase 6 (CMIP6, Feng et al.,
184   2020). Climatological biogenic emissions are from the Chemistry-Climate Model Initiative (CCMI;
185   Morgenstern et al., 2017) but isoprene and monoterpene emissions are annually varying from the
186   Joint UK Land Environment Simulator (JULES, Pacifico et al., 2011) within the free-running UK Earth
187   System Model (UKESM Sellar et al., 2019) from a CMIP6 historical setup. Other natural emissions
188   come from the Precursors of Ozone and their Effects in the Troposphere (POET, Olivier et al., 2003)
189   and biomass burning emissions from the Global Fire Emissions Database (GFED) version 4 (van der
190   Werf et al., 2017). For methane (CH_4), the model tracer is scaled to the annually varying global
191   averaged surface CH_4 value from NOAA (Dlugokencky, 2020). The model was spun up for 1-year
192   (2007) and the model tracers output daily at 09:30 local time (LT) globally to match the MetOp-A
193   daytime overpass time. When comparing with IASI, the satellite AKs are applied to the TOMCAT
194   vertical ozone profiles in the same way as the ozonesondes (i.e. **Equation 1**). Here, the TOMCAT
195   ozone profile (already temporally co-located) is co-located from the model grid box the retrieval sits
196   in. To investigate the importance of emissions and meteorology on TO_3 and TO_3RE, two sensitivity
197   experiments were run between 2008 and 2017 using repeating emissions and meteorology for 2008
198   (i.e. start of the time-series) annually in the model simulation over the time period.

2.4. Radiative Transfer Model and Kernel

200   The TO_3RE was calculated using a radiative kernel, derived from the SOCRATES off-line radiative
201   transfer model (Edwards and Slingo, 1996), in combination with TOMCAT and the three IASI ozone
202   products. SOCRATES has six bands in the short-wave and nine in the long-wave. Meteorological
203   inputs (temperature, water vapour, surface albedo) into SOCRATES to derive the radiative kernel are
204   based on climatological ECMWF ERA-Interim reanalysis. Cloud fields are based on 2000 data from
205   International Satellite Cloud Climatology Project data (Rossow and Schiffer, 1999), while aerosols
206   have been ignored. To account for stratospheric temperature adjustments, Rap et al., (2015) used
207   the dynamical heating approximation (Fels et al., 1980). This involved accounting for changes in the

208   stratospheric heating rate determined from the model due to the O_3 perturbation, which were
209   applied to the temperature field, with the model run iteratively until stratospheric temperatures
210   reached equilibrium (Rap et al., 2015). This approach of using the SOCRATES off-line radiative kernel
211   with output from model simulations to derive the TO_3 radiative effect has been used in several
212   studies e.g. Rap et al., (2015), Scott et al., (2018), Iglesias-Suarez et al. (2018) and Rowlinson et al.,
213   (2020).

214   To derive the satellite TO_3RE, the annual average IASI 3D ozone field is multiplied by the off-line
215   radiative kernel (grid box by grid box) and then summed from the surface to the tropopause
216   pressure. Here, the IASI ozone data is mapped onto the spatial resolution of the radiative kernel and
217   then interpolated vertically onto its pressure grid. The equation for each grid box is:

218    $$TO_3RE = \sum_{i=surf}^{trop} RK_i \times O_{3i} \times dp_i/100 \qquad (2)$$

219   where TO_3RE is the tropospheric ozone radiative effect (W/m^2), RK is the radiative kernel
220   (W/m^2/ppbv/100 hPa), O_3 is the satellite ozone grid box value (ppbv), dp is the pressure difference
221   between vertical levels (hPa) and i is the grid box index between the surface pressure level and the
222   tropopause pressure. The tropopause pressure is based on the World Meteorological Organisation
223   (WMO) definition of "the lowest level at which the temperature lapse rate decreases to 2 K/km or
224   less" (WMO, 1957).

225   **3. Results**

226   **3.1.   Tropospheric Ozone Radiative Effect**

227   **Figure 1** shows the IASI derived TCO_3, TO_3RE and normalised TO_3RE (NTO_3RE, i.e. the TO_3RE divided
228   by its TCO_3 as in Rap et al., (2015)). For the TCO_3, the three harmonised IASI products have good
229   spatial agreement in the decadal (2008-2017) average, with a background north-south hemisphere
230   gradient of approximately 30.0-40.0 to 15.0-25.0 DU. Peak TCO_3 (>40.0 DU) occurs over East Asia,
231   the Middle East and in ozone outflow from central Africa (e.g. production from lightning and
232   biomass burning precursor gases (Moxim & Levy, 2000)). The global average TCO_3 values for IASI-
233   FORLI, IASI-SOFRID and IASI-IMS are 32.6 DU, 29.9 DU and 29.9 DU, respectively (**Figure 1 left**
234   **column** and **Table 1**). From **Table 1**, degrees of freedom of signal (DOFS) are approximately 1.0 for
235   the troposphere (i.e. DOFS$_{trop}$) and also in the upper troposphere – lower stratosphere (UTLS,
236   DOFS$_{utls}$) – i.e. the vertical region where the O_3 radiative effect is most prominent). These DOFS are
237   derived on a global scale using IASI data for 2008. They show there to be sufficient information in
238   the troposphere from IASI to derive radiative effect metrics. Therefore, like in Rap et al., (2015), we
239   are confident in our approach to directly use the satellite data to derive the observational TO_3RE.

240   When the TO_3RE is calculated (**Figure 1 middle column**), peak values occur over the sub-tropics,
241   Africa and Australia ranging consistently between approximately 2.0 and 2.5 W/m^2 for each IASI
242   product. The minimum values are found at high latitudes ranging between 0.0 and 0.8 W/m^2. The
243   bottom panel of **Figure 1** shows the zonally average profiles weighted by the cosine of latitude
244   (similar to Rap et al., 2015). This accounts for area weighting in the derived TO_3RE for different
245   latitude bands on the global weighted average. Here, TCO_3 is near-zero at high-latitudes,
246   approximately 15.0-20.0 DU at mid-latitudes, peaking at 28.0-33.0 DU in the sub-tropics and then
247   decreasing by several DU in the tropics. The corresponding TO_3RE profiles follow a similar pattern
248   with near-zero values at high-latitudes, approximately 0.5-1.0 W/m^2 at mid-latitudes, peaking at 1.5
249   W/m^2 in the sub-tropics and then decreasing to 1.1-1.2 W/m^2 in the tropics. Therefore, the sub-

250 tropics have the largest contribution to the global TO_3RE. The global weighted TO_3RE averages for
251 IASI-FORLI, IASI-SOFRID and IASI-IMS are 1.23, 1.21 and 1.21 W/m^2, respectively (**Figure 1** and **Table
252 1**).

253 The NTO_3RE (**Figure 1 right column**) provides an estimate of where the TO_3RE is most sensitive to
254 changes in TCO_3 (i.e. the unit of TO_3RE per unit of TCO_3). Peak NTO_3RE (>50.0 $mW/m^2/DU$) occurs at
255 similar locations to the peak TO_3RE (e.g. Africa and Australia), while the minimum values (10.0-20.0
256 $mW/m^2/DU$) occur at high-latitudes. Over the sub-tropical oceans, there are NTO_3RE values of
257 similar magnitude (approximately 45.0 $mW/m^2/DU$). Therefore, despite some regions having lower
258 TCO_3 and TO_3RE values (e.g. the South Pacific vs. the South Atlantic and Indian Ocean), the sensitivity
259 to ozone perturbations (i.e. radiative effect per unit of TO_3) is similar in these regions.

260 Overall, the global weighted average NTO_3RE is 37.78, 40.43 and 40.60 $mW/m^2/DU$ for IASI-FORLI,
261 IASI-SOFRID and IASI-IMS, respectively. It is likely that differences between the three ozone retrieval
262 schemes could be causing the differences between globally averaged NTO_3RE values. As the IASI-
263 FORLI NTO_3RE is lower, while having the highest global average TCO_3 and TO_3RE, it suggests that
264 IASI-FORLI has a larger fraction of TO_3 is located in the mid-troposphere, where the radiative kernel
265 has less sensitivity than the upper troposphere. Further to this, as the IASI ozone products only have
266 approximately 1.0 DOFS in the troposphere (**Table 1**), the harmonisation of the products using the
267 ozonesondes can best be done on a tropospheric column level. As a result, the scaling of the satellite
268 derived TO_3RE is done based on the relationship between the original IASI and IASI-sonde corrected
269 TCO_3. Thus, a limitation being that though the upper troposphere is the most sensitive region to
270 ozone radiative properties, the scaling of the TO_3RE is applied based on the satellite-ozonesonde
271 TCO_3 relative differences.

272 TOMCAT allows for a further quantification of the TO_3RE in the satellite-era and the ability to run
273 sensitivity experiments to explore some important top-level processes. Evaluation of the model
274 using the IASI products and ozonesondes (see **SI-2**, **Figure S3** & **S4**) shows the model generally
275 captures the TCO_3 spatial pattern and absolute values. In the tropics (mid/high-latitudes), the model
276 underestimates (overestimates) by approximately 10-20% on average. These biases are comparable
277 with other modelling studies evaluating models against satellite TO_3 observations (e.g. Archibald et
278 al., 2020; Monks et al., 2017; Nassar et al., 2009; Young et al., 2013), indicating TOMCAT to be
279 suitable for this study.

280 The global mean TCO_3 from TOMCAT (2008-2017) (**Figure 2 – top panel**) is 30.7 DU and consistent
281 with the IASI data sets in **Figure 1**. When translated into TO_3RE, described above, the peak values
282 from TOMCAT range between 2.0 and >2.5 W/m^2 over Africa, Australia and the sub-tropics. The
283 global area-weighted TO_3RE for TOMCAT is 1.26 W/m^2, thus slightly larger than for IASI (1.21-1.23
284 W/m^2). As TOMCAT has a positive TCO_3 bias with respect to the observations in the sub-tropics,
285 where the TO_3RE influence is most pronounced, this probably explains the slightly larger model
286 TO_3RE value. In the bottom panel of **Figure 2**, the zonal profiles (weighted by cosine of latitude to
287 highlight the relative influence on the global weighted average) for TCO_3 (TO_3RE) have similar values
288 to that of IASI. Here, the TOMCAT high-latitude values are near-zero (constrained by $\cos(90^o) = 0$),
289 mid-latitude values range between 10.0 and 20.0 DU (0.5 to 1.0 W/m^2) and sub-tropical values range
290 between 30.0 and 38.0 DU (1.5 and 1.7 W/m^2). There is a decrease to approximately 25.0 DU (1.0-
291 1.3 W/m^2) in the tropics. In terms of the NTO_3RE, the TOMCAT global area-weighted average is 41.0

292   mW/m^2/DU, which is similar to IASI. The peak NTO$_3$RE values are over the oceans (50.0-60.0
293   mW/m^2/DU) and over Africa/Australia (>60.0 mW/m^2/DU).

294   **3.2.**   **Temporal Evolution of the Tropospheric Ozone Radiative Effect**

295   As IASI has daily global coverage (Clerbaux et al., 2009), we are able to derive annual average 3D
296   ozone fields between 2008 and 2017, thus providing the first assessment of interannual variability
297   and decadal tendency in satellite derived TO$_3$RE. **Figure 3** shows the annual TO$_3$RE time series for all
298   three IASI products. First thing to note is that the Eumetsat meteorological data used to retrieve
299   ozone for the IASI-FORLI product is subject to discontinuities (Boynard et al., 2018; Wespes et al.,
300   2018). As a result, we include decadal analysis of the IASI-FORLI data for the full time period (2008-
301   2017) and then a sub-time period (2011-2017) given the large discontinuity in September 2010
302   reported by Boynard et al., (2018) and Wespes et al., (2018). Here, we can derive the TO$_3$RE to
303   quantify the absolute values and how they compare between products over the two time periods. In
304   the near future, a new consistent IASI-FORLI ozone climate data record will be available using a more
305   stable set of level-2 Eumetsat meteorological data retrieved from MetOp IASI and microwave
306   sounders.

307   For IASI-SOFRID and IASI-IMS, the annual TO$_3$RE values range between 1.19 and 1.24 W/m^2 across
308   the 2008-2017 decade. IASI-FORLI has somewhat larger values at the start of the record (1.26-1.28
309   W/m^2) before tending to that of IASI-SOFRID/IASI-IMS from 2011 onwards. Correlations (squared) in
310   the annual TO$_3$RE time-series between IASI-FORLI and IASI-SOFRID (IASI-IMS) are poor at R^2=0.148
311   (R^2=0.132). However, IASI-SOFRID and IASI-IMS have a much stronger agreement with R^2=0.591
312   sharing nearly 60% of the temporal variability. We also calculate the coefficient of variation (CoV,
313   i.e., time series standard deviation divided by its mean) to assess the inter-annual variability. For
314   IASI-SOFRID and IASI-IMS, this is 1.1%, but for IASI-FORLI it is 2.5%. Therefore, there is more year-to-
315   year variability in the IASI-FORLI TO$_3$RE record. However, when focussing on IASI-FORLI data for
316   2011-2017, the CoV drops to 1.2% in-line with IASI-SOFRID and IASI-IMS. The correlation (squared)
317   values are now R$^2_{FORLI-SOFRID}$=0.496 and R$^2_{FORLI-IMS}$=0.137, which shows improved agreement between
318   IASI-FORLI and IASI-SOFRID, but slightly surprisingly not with IASI-IMS. This may potentially be due to
319   the lower sampling sizes of the IASI-IMS data record. Using ordinary least squares fit regression, IASI-
320   FORLI, IASI-SORFRID and IASI-IMS have global average weighted TO$_3$RE linear trends of -0.64 (-0.99, -
321   0.28; 95% confidence interval) %/year, -0.01 (-0.14, 0.12) %/year and -0.13 (-0.36, 0.10) %/year (see
322   **Table 1**). As the IASI-FORLI product has known discontinuities (hence the larger CoV), the near-zero
323   IASI-SOFRID and IASI-IMS trends are more robust. This is supported by IASI-FORLI when only
324   considering 2011-2017 with a linear trend of -0.21 (-0.66, 0.23) %/year. Therefore, this suggests
325   negligible change in the contribution of TO$_3$ to the tropospheric radiative effect over the recent past
326   (i.e. 2008-2017).

327   TOMCAT global average weighed TO$_3$RE ranges between 1.24 and 1.29 W/m^2 between 2008 and
328   2017. The CoV is 1.5% for TOMCAT and is comparable to the IASI products (i.e. IASI-FORLI for later
329   years). The TOMCAT TO$_3$RE time-series also has similar temporal variability (e.g. peaks in 2008, 2010
330   and 2017 and troughs in 2009 and 2014 to that of the IASI products. The underlying TOMCAT TO$_3$RE
331   decadal trend is -0.05 (-0.40, 0.30) %/year and consistent with the IASI products. So, between 2008
332   and 2017, there has been limited overall change in TO$_3$, despite reasonable interannual variability,
333   and thus its decadal impact on the TO$_3$RE has been relatively minor.

334   To investigate the importance of emissions and meteorology on the decadal TO$_3$RE trends, TOMCAT
335   was run twice for the full time-period, once using repeating emissions and once using repeating
336   meteorology for 2008 (i.e. start of the time-series). Using fixed emissions reduced the TO$_3$ burden
337   and the TO$_3$RE values dropped to 1.22 to 1.28 W/m^2 (i.e. minima in 2014 and 2015 more
338   pronounced). However, the trend in TO$_3$RE (-0.23 (-0.59, 0.23) %/year) remained small indicating
339   that temporal changes in emissions yield a relatively small influence on the decadal tendency in
340   TO$_3$RE. By comparison with the fixed meteorology run, temporal changes in meteorological
341   processes over the period 2008-17 were found not to dramatically alter the TO$_3$RE values either, but
342   there is an increase to 1.26 to 1.30 W/m^2 when the model meteorology is fixed to 2008. The
343   corresponding TO$_3$RE trend in the fixed meteorology run is 0.26 (0.13, 0.39) %/year leading to a
344   steady increase in TO$_3$RE, though with a similar magnitude to that of the fixed emissions experiment.
345   Therefore, temporal changes in pre-cursor emissions and meteorological processes appear to be
346   balancing each other leading to the near-zero TOMCAT control run TO$_3$RE trend. However, the
347   largest changes in TO$_3$RE between the control and fixed meteorology runs are towards the end of
348   the decade, coinciding with the 2015/2016 El Niño event (i.e. TO$_3$ spatiotemporal variability has
349   previously been linked to El Niño activity – e.g. Ziemke et al., (2015) and Rowlinson et al., (2019)).
350   The largest difference between the TOMCAT control and fixed meteorology runs is 0.6 W/m^2 in
351   2015, large El Niño year. Overall, the year-to-year variability in meteorology appears to be
352   contracting any decadal TO$_3$RE trend arising from temporal changes in precursor emissions with the
353   net result being no substantial underlying change in TO$_3$RE over the 2008-2017 decade.

354   **Figure 4** shows the horizontal and vertical impact of the two sensitivity experiments on TOMCAT O$_3$
355   radiative effect (note the different colour bar scales). Consistent with **Figures 1** and **2**, the TOMCAT
356   control TO$_3$RE has peak values (>2.50 W/m^2) over northern Africa and throughout the sub-tropics
357   (approximately 2.0 W/m^2, **Figure 4a**). Vertically, the TOMCAT peak ozone radiative effect (>0.25
358   W/m^2) is in the upper troposphere (**Figure 4b**) with the largest impact in the sub-tropics of both
359   hemispheres (500-200 hPa). Similar values extend through mid-latitudes of both hemispheres but in
360   a smaller pressure range (400-300 hPa).

361   In **Figure 4c**, TO$_3$RE is seen to be higher in the fixed meteorology run than the control by 0.1 to >0.2
362   W/m^2 throughout the tropics and sub-tropics, although there is considerable spatial variability,
363   including an area in the sub-tropical Pacific where TO$_3$RE is lower in the fixed meteorology run by -
364   0.15 W/m^2. In high and mid-latitudes, TO$_3$RE is lower than the control by between -0.1 and 0.0
365   W/m^2. In the upper troposphere (**Figure 4d**), the zonal averaged contribution to TO$_3$RE in the fixed
366   meteorology run is consistently higher than the control, by up to 0.02 W/m^2 at approximately 200
367   hPa in the tropics and sub-tropics and persisting at approximately 0.01 W/m^2 down to 600 hPa in the
368   same latitudinal range. Poleward of 50°N and 50°S, TO$_3$RE is lower in the fixed meteorology run,
369   peaking at -0.02 to -0.015 W/m^2 at 300 hPa and extending down to 500 hPa at -0.005 W/m^2.

370   With fixed emissions, TO$_3$RE is higher at northern mid- and high latitudes by up to 0.02 W/m^2,
371   whereas in the tropics/sub-tropics and southern mid-latitudes it is generally lower than in the
372   control run by up to -0.02 W/m^2 (**Figure 4e**). However, over tropical Asia, Indonesia and Australia,
373   TO$_3$RE is seen to be lower by a more substantial amount, -0.05 to -0.04 W/m^2. In regard to its height
374   dependence, contributions to TO$_3$RE are seen in **Figure 4f** to be lower in the fixed emissions run by
375   up to -0.005 W/m^2 in the tropics/sub-tropics between 600 and 200 hPa, and also in a tongue
376   stretching to southern high latitudes at around 300hPa (**Figure 4f**). In the northern hemisphere, on

377 the other hand, TO$_3$RE in the layer between 400 and 600 hPa is seen to be higher by up to 0.003 at
378 latitudes from the pole to 50°N, and down to higher pressures at latitudes below 50°N.

379 In summary, the two model sensitivity experiments indicate that, except for southern high latitudes,
380 precursor emissions and meteorology exerted counteracting influences of comparable magnitude on
381 TO$_3$RE in the 2008-17 decade, and this is specifically so in the sub-tropical regions of the upper
382 troposphere, where contributions to global average area weighted TO$_3$RE are largest. At southern
383 high latitudes, precursor emissions and meteorology are seen to have both increased TO$_3$RE over
384 this period, specifically through contributions in the uppermost troposphere, although area
385 weighting minimized their combined impact in the global averaged TO$_3$RE.

4. Conclusions

387 By using state-of-the-art satellite ozone profile retrievals from the Infrared Atmospheric Sounding
388 Interferometer (IASI), on-board MetOp-A, in combination with the TOMCAT chemical transport
389 model (CTM) and the offline radiative transfer model, SOCRATES, we provide an updated estimate of
390 the tropospheric ozone radiative effect (TO$_3$RE) and provide the first observational constraint on its
391 variability over the decade 2008-2017. Building upon the previous study of Rap et al., (2015), who
392 quantified the globally weighed average TO$_3$RE to be 1.17±0.03 W/m^2 (based on data between 2005
393 and 2008), we find the decadal average TO$_3$RE, between 2008 and 2017, to range from 1.21 and 1.26
394 W/m^2. This represents an update on the estimates from Rap et al., 2015 using an improved version
395 of the TOMCAT model (as in Monks et al., (2017) compared to Richards et al., 2013)) and improved
396 satellite products with better spatial and temporal coverage. However, these two studies do cover
397 different time periods, which may be contributing to the differences between the studies. Secondly,
398 neither the modelled, nor the observed TO$_3$RE suggest any substantial change during this decade.
399 Investigations of the importance of ozone precursor emissions and meteorology, through targeted
400 sensitivity experiments repeating emissions and meteorology for 2008 (i.e. year at start of time-
401 series), suggest that temporal changes in both factors have counteracted each other. Fixing
402 emissions reduces the TO$_3$RE values/tendency, so changes in emissions are driving a steady increase
403 in the TO$_3$RE. Conversely, fixing the meteorology drives an increase in the TO$_3$RE values/tendency,
404 thus is yielding to a net decrease in TO$_3$RE despite its large variability. Therefore, the net
405 tropospheric ozone contribution to atmospheric radiative properties, and potentially climate, has
406 remained relatively stable with time during 2008-2017.

Acknowledgements

408 This work was funded by the UK Natural Environment Research Council (NERC) by providing funding
409 for the National Centre for Earth Observation (NCEO, award reference NE/R016518/1) and funding
410 from the European Space Agency (ESA) Climate Change Initiative (CCI) post-doctoral fellowship
411 scheme (award reference 4000137140). The TOMCAT runs were undertaken on ARC3, part of
412 the High-Performance Computing facilities at the University of Leeds, UK. The IASI-SOFRID
413 research was conducted at LAERO with some financial support from the CNES French spatial agency
414 (TOSCA–IASI project). We thank the AC SAF project of the EUMETSAT for providing data and/or
415 products used in this paper. Anna Maria Trofaier (ESA Climate Office) provided support and advice
416 throughout the fellowship.

417

418

Data Availability

The IASI-FORLI and IASI-SOFRID data can be obtained from https://iasi.aeris-data.fr/O3 and https://iasi-sofrid.sedoo.fr/. The IASI-IMS data is available via the NERC Centre for Environmental Data Analysis (CEDA) Jasmin platform subject to data requests. However, the IASI-IMS data and TOMCAT simulations used in this study are available from https://homepages.see.leeds.ac.uk/~earrjpo/to3re/. The ozonesonde data for WOUDC, SHADOZ and NOAA is available from https://woudc.org/, https://tropo.gsfc.nasa.gov/shadoz/ and https://gml.noaa.gov/ozwv/ozsondes/.

Author Contributions

RJP conceptualised, planned and undertook the research study. AR provided the SOCRATES radiative kernel. BB, ELF, BJK, RS, BGL, LJV, AB and CW provided the IASI ozone data and advice on using the products. MAP performed the TOMCAT model simulations with support from MPC and WF. CR provided advice and help during RP's ESA CCI fellowship. RJP prepared the manuscript with contributions from all co-authors.

Conflicts of Interest

The authors declare no conflicts of interest.

References

Archibald, A.T., O'Connor, F.M., Abraham, N.A., et al. 2020. Description and evaluation of the UKCA stratosphere–troposphere chemistry scheme (StratTrop vn 1.0) implemented in UKESM1. *Geoscientific Model Development*, **13**, 1223–1266, doi: 10.5194/gmd-13-1223-2020.

Barret, B., Le Flochmoen, E., Sauvage, B., et al. 2011. The detection of post-monsoon tropospheric ozone variability over south Asia using IASI data. *Atmospheric Chemistry and Physics*, **11**, 9533-9548, doi: 10.5194/acp-11-9533-2011.

Barret, B., Emili, E., Le Flochmoen, E. 2020. A tropopause-related climatological a priori profile for IASI-SOFRID ozone retrievals: improvements and validation. *Atmospheric Measurement Techniques*, **13**, 5237–5257, doi: 10.5194/amt-13-5237-2020.

Bowman, K.W., Shindell, D.T., Worden, H.M., et al. 2013. Evaluation of ACCMIP outgoing longwave radiation from tropospheric ozone using TES satellite observations. *Atmospheric Chemistry and Physics*, 13, 4057-4072, doi: 10.5194/acp-13-4057-2013.

Boynard, A., Hurtmans, D., Garane, K., et al. 2018. Validation of the IASI FORLI/EUMETSAT ozone products using satellite (GOME-2), ground-based (Brewer-Dobson, SAOZ, FTIR) and ozonesonde measurements. *Atmospheric Measurement Techniques*, **11 (9)**, doi: 10.5194/amt-11-5125-2018.

Chipperfield, M.P. 2006. New version of the TOMCAT/SLIMCAT off-line chemistry transport model: Intercomparison of stratospheric trace experiments. *Quarterly Journal of the Royal Meteorological Society*, **132**, 1179–1203, doi:10.1256/qj.05.5.

Clerbaux, A., Boynard, A., Clarisse, L., et al. 2009. Monitoring of atmospheric composition using the thermal infrared IASI/MetOp sounder. *Atmospheric Chemistry and Physics*, **9**, 6041–6054, doi: 10.5194/acp-9-6041-2009.

Dee, D.P., Uppala, S.M., Simmons, A.J., et al.: The ERA-Interim reanalysis: Configuration and performance of the data assimilation system, *Quarterly Journal of the Royal Meteorological Society*, 137 (656), 553–597, doi:10.1002/qj.828, 2011.

Dlugokencky, E. 2020. NOAA Global Monitoring Laboratory–Trends in Atmospheric Methane, Available at: https://gml.noaa.gov/ccgg/trends_ch4/ (last accessed 23/01/2023).

Doniki, S., Hurtmans, D., Clarisse, et al. 2015. Instantaneous longwave radiative impact of ozone: an application on IASI/MetOp observations, *Atmospheric Chemistry and Physics*, **15**, 12971–12987, doi:10.5194/acp-15-12971-2015.

Edwards, J.M and Slingo, A. 1996. Studies with a flexible new radiation code. I: Choosing a configuration for a large-scale model. *Quarterly Journal of the Royal Meteorological Society*, **122**, 689–719, doi:10.1002/qj.49712253107.

Fels, S.B., Mahlman, J.D., Schwarzkopf, M.D., et al. 1980. Stratospheric Sensitivity to Perturbations in Ozone and Carbon Dioxide: Radiative and Dynamical Response. *Journal of Atmospheric Science*, **37**, 2265-2297, doi: 10.1175/1520-0469(1980)037<2265:Sstpio>2.0.Co;2.

Feng, L., Smith, S. J., Braun, C., et al. 2020. The generation of gridded emissions data for CMIP6. *Geoscientific Model Development*, **13**, 461–482, doi:10.5194/gmd-13-461-2020.

Fleming ZL, Doherty RM, von Schneidemesser E, Malley CS, Cooper OR, Pinto JP, Colette A, Xutt X, Simpson D, Schultz MG, Lefohn AS, Hamad S, Moolla R, Solberg S and Feng Z.: Tropospheric Ozone Assessment Report: Present-day ozone distribution and trends relevant to human health. *Elem Sci Anth*, **6**(12), doi: 10.1525/elementa.273, 2018.

Forster, P., Storelvmo, T., Armour, K., Collins, W., Dufresne, J.- L., Frame, D., Lunt, D. J., Mauritsen, T., Palmer, M. D., Watanabe, M., Wild, M., and Zhang, H.: The Earth's Energy Budget, Climate Feedbacks, and Climate Sensitivity, in: Climate Change 2021: The Physical Science Basis, Contribution of Working Group I to the Sixth Assessment Report of the Intergovernmental Panel on Climate Change, edited by: Masson-Delmotte, V., Zhai, P., Pirani, A., Connors, S. L., Péan, C., Berger, S., Caud, N., Chen, Y., Goldfarb, L., Gomis, M. I., Huang, M., Leitzell, K., Lonnoy, E., Matthews, J. B. R.,Maycock, T. K., Waterfield, T., Yelekçi, O., Yu, R., and Zhou, B., Cambridge University Press, Cambridge, United Kingdom and New York, NY, USA, 923– 1054, doi:10.1017/9781009157896.009, 2021.

Gauss, M., Myhre, G., Isaksen, S.A., et al. 2006. Radiative forcing since preindustrial times due to ozone change in the troposphere and the lower stratosphere. *Atmospheric Chemistry and Physics*, **6**, 575-599, doi: 10.5194/acp-6-575-2006.

Gulev, S.K., P.W. Thorne, J. Ahn, F.J. Dentener, C.M. Domingues, S. Gerland, D. Gong, D.S. Kaufman, H.C. Nnamchi, J. Quaas, J.A. Rivera, S. Sathyendranath, S.L. Smith, B. Trewin, K. von Schuckmann, and R.S. Vose.: Changing State of the Climate System. In Climate Change 2021: The Physical Science Basis. Contribution of Working Group I to the Sixth Assessment Report of the Intergovernmental Panel on Climate Change, edited by Masson-Delmotte, V., P. Zhai, A. Pirani, S.L. Connors, C. Péan, S. Berger, N. Caud, Y. Chen, L. Goldfarb, M.I. Gomis, M. Huang, K. Leitzell, E. Lonnoy, J.B.R. Matthews, T.K. Maycock, T. Waterfield, O. Yelekçi, R. Yu, and B. Zhou., Cambridge University Press, Cambridge, United Kingdom and New York, NY, USA, pp. 287–422, doi:10.1017/9781009157896.004, 2021.

496 Heue, K.P., Cold-Egbers, M., Delcloo, A., et al. 2016. Trends of tropical tropospheric ozone from 20
497 years of European satellite measurements and perspectives for the Sentinel-5 Precursor.
498 *Atmospheric Measurement Techniques*, **9**, 5037-5051, doi: 10.5194/amt-9-5037-2016.

499 Hurtmans, D., Coheur, P.-F., Wespes, C., et al. 2012. FORLI radiative transfer and retrieval code for
500 IASI, *Journal of Quantitative Spectroscopy and Radiative Transfer*, **113**, 1391–1408,
501 doi:10.1016/j.jqsrt.2012.02.036. Iglesias-Suarez, F., Kinnison, D.E., Rap, A., et al. 2018. Key drivers of
502 ozone change and its radiative forcing over the 21st century. *Atmospheric Chemistry and Physics*, **18**,
503 6121-6139, doi:10.5194/acp-18-6121-2018.

504 IASI-IMS. 2022. IASI-IMS Data [Dataset],
505 https://homepages.see.leeds.ac.uk/~earrjpo/to3re/iasi_ims/ (last accessed 01/01/2023).

506 IASI-FORLI. 2020. Daily IASI/Metop-A ULB-LATMOS ozone (O3) L2 product (total column and
507 vertical profile) (v20151001) [Dataset], https://iasi.aeris-data.fr/catalog/ (last accessed
508 15/12/2022).

509 IASI-SOFRID. 2022. Welcome to the IASI-SOFRID database (vn3.5) [Dataset],
510 http://thredds.sedoo.fr/iasi-sofrid-o3-co/ (last accessed 01/12/2022).

511 Iglesias-Suarez, F., Kinnison, D.E., Rap, A., et al. 2018. Key drivers of ozone change and its radiative
512 forcing over the 21st century. *Atmospheric Chemistry and Physics*, **18**(9), 6121-6139, doi:
513 10.5194/acp-18-6121-2018.

514 Joiner, J., Schoeberl, R.M., Vasilkov, A.P., et al. 2009. Accurate satellite-derived estimates of the
515 tropospheric ozone impact on the global radiation budget. *Atmospheric Chemistry and Physics*, **9**,
516 4447-4465, doi: 10.5194/acp-9-4447-2009.

517 Keppins, A., Lambert, J.C., Granville, J., et al. 2018. Quality assessment of the Ozone_cci Climate
518 Research Data Package (release 2017) – Part 2: Ground-based validation of nadir ozone profile data
519 products. *Atmospheric Measurement Techniques*, **11**, 3769-3800, doi: 10.5194/amt-11-3769-2018.

520 Lamarque, J.F., Bond, T.C., Eyring, V., et al. 2010. Historical (1850-2000) gridded anthropogenic and
521 biomass burning emissions of reactive gases and aerosols: methodology and application.
522 *Atmospheric Chemistry and Physics*, **10**, 7017-7039, doi: 10.5194/acp-10-7017-2010.

523 Mann, G.W., Carslaw, K.S., Spracklen, D.V., et al. 2010. Description and evaluation of GLOMAP-
524 mode: A modal global aerosol microphysics model for the UKCA composition-climate
525 model. *Geoscientific Model Development*, **3**(2), 519– 551, doi:10.5194/gmd-3-519-2010.

526 McPeters, R.D., Labow, G.J., and Logan, J.A. 2007. Ozone climatological profiles for satellite retrieval
527 algorithms. *Journal of Geophysical Research*, **112** (D05308), https://doi.org/10.1029/2005JD006823.

528 Mills G, Pleijelt H, Malley CS, Sinha B., Cooper OR, Schultz MG, Neufeld HS, Simpson D, Sharps K,
529 Feng Z, Gerosa G, Harmens H, Kobayashi K, Saxena P, Paoletti E, Sinha V and Xu X.: Tropospheric
530 Ozone Assessment Report: Present-day tropospheric ozone distribution and trends relevant to
531 vegetation. *Elem Sci Anth*, 6(47), doi: 10.1525/elementa.302, 2018.

532 Monks, S.A., Arnold, S.R., Hollaway, M.J., et al. 2017. The TOMCAT global chemistry transport model
533 v1.6: Description of chemical mechanism and model evaluation. *Geoscientific Model
534 Development*, **10**(8), 3025– 3057, doi:0.5194/gmd-10-3025-2017.

535 Morgenstern, O., Hegglin, M.I., Rozanov, E., et al. 2017. Review of the global models used with phase
536 1 of the Chemistry-Climate Model Initiative (CCMI). *Geoscientific Model*
537 *Development*, **10**(2), 639– 671, doi:10.5194/gmd-10-639-2017.

538 Moxy, W.J. and Levy, H. 2000. A model analysis of tropical South Atlantic Ocean tropospheric ozone
539 maximum: The interaction of transport and chemistry. *Journal of Geophysical Research*, **105** (D13),
540 17393-17415, doi:10.1029/2000JD900175.

541 Myhre, G., Shindell, D., Breon, F.M., et al. 2013. Anthropogenic and Natural Radiative Forcing, in:
542 Climate Change 2013: The Physical Science Basis. Contribution of Working Group I to the Fifth
543 Assessment Report of the Intergovernmental Panel on Climate Change Cambridge University Press,
544 Cambridge, United Kingdom and New York, NY, USA, 659–740.

545 Nassar, R., Logan, J.A., Mergretskaia, I.A., et al. 2009. Analysis of tropical tropospheric ozone, carbon
546 monoxide, and water vapor during the 2006 El Niño using TES observations and the GEOS-Chem
547 model. *Journal of Geophysical Research: Atmospheres*, **114 (D17304)**, doi: 10.1029/2009JD011760.

548 NOAA. 2023. ESRL/GML Ozonesondes [Dataset], https://gml.noaa.gov/ozwv/ozsondes/ (last
549 accessed 01/06/2022).

550 Olivier, J., Peters, J., Granier, C., et al. 2003. Present and future surface emissions for atmsopheric
551 compounds, *POET report #2*, Available at: http://accent.aero.jussieu.fr/Documents/del2_final.doc
552 (last accessed 23/01/2023).

553 Pacifico, F., Harrison, S.P., Jones, C.D., et al. 2011. Evaluation of a photosynthesis-based biogenic
554 isoprene emission scheme in JULES and simulation of isoprene emissions under present-day climate
555 conditions, *Atmospheric Chemistry and Physics,* **11**, 4371–4389, doi**:**10.5194/acp-11-4371-2011.

556 Pimlott, M.A., Pope, R.P., Kerridge, B.J., et al. 2022. Investigating the global OH radical distribution
557 using steady-state approximations and satellite data. *Atmospheric Chemistry and Physics,* **22**, 10467-
558 10488, doi: 10.5194/acp-22-10467-2022.

559 Pope, R.J., Kerridge, B.J., Siddans, R., Latter, B.G., Chipperfield, M.P., Arnold, S.R., Ventress, L.J.,
560 Pimlott, M.A., Graham, A.M., Knappett, D.S and Rigby R.: Large Enhancements in Southern
561 Hemisphere Satellite-Observed Trace Gases Due to the 2019/2020 Australian Wildfires. *Journal of*
562 *Geophysical Research: Atmospheres,* **126**(18), e2021JD034892, doi: 10.1029/2021JD034892, 2021.

563 Rap, A., Richard, N.A.D., Forster, P.M., et al. 2015. Satellite constraint on the tropospheric ozone
564 radiative effect. *Geophysical Research Letters*, **42**, 5074–5081, doi: 10.1002/2015GL064037.

565 Richards, N.A.D, Osterman, G.B., Browell, E.V., et al. 2008. Validation of tropospheric emission
566 spectrometer ozone profiles with aircraft observations during the intercontinental chemical
567 transport experiment–B. *Journal Geophysical Research*, **113**(D16S29), doi: 10.1029/2007JD008815.

568 Rodgers, C.D. 2000. Inverse methods for atmospheric sounding: Theory and practice. New Jersey,
569 USA: World Science.

570 Rossow, W.B. and Schiffer, R.A.: Advances in understanding clouds from ISCCP, *Bulletin of the*
571 *American Meteorological Society*, **80**(11), 2261–2287, doi:10.1175/1520-
572 0477(1999)080>2.0.co;2,1999.

573 Rowlinson, M.J., Rap, A., Arnold, S.R., Pope, R.J., Chipperfield, M.P., McNorton, J., Forster, P., Gordon,
574 H., Pringle, K.J., Feng, W., Kerridge, B.J., Latter, B.G., Siddans, R.: Impact of El Nino-Southern Oscillation

575 on the interannual variability of methane and tropospheric ozone. Atmospheric Chemistry and
576 Physics, **19** (13), 8669-8686, doi: 10.5194/acp-19-8669-2019, 2019.

577 Rowlinson, M.J., Rap, A., Hamilton, D.S., et al. 2020. Tropospheric ozone radiative forcing uncertainty
578 due to pre-industrial fire and biogenic emissions. *Atmospheric Chemistry and Physics*, **20**, 10937-
579 10951, doi: 10.5194/acp-20-10937-2020.

580 Saunders, R., Matricardi, M., and Brunel, P. 1999. An improved fast radiative transfer model for
581 assimilation of satellite radiance observations. *Quarterly Journal of the Royal Meteorological Society*,
582 **125** (556 part B), 1407–1425, doi:10.1256/smsqj.55614.

583 Scott, C.E., Monks, S.A., Spracklen, D.V., et al. 2018. Impact on short-lived climate forcers increases
584 projected warming due to deforestation. *Nature Communications*, **9**, 157, doi: 10.1038/s41467-017-
585 02412-4.

586 Sellar, A.A., Jones, C.G., Mulcahy, J.P., et al. 2019. Description and Evaluation of the UK Earth System
587 Model. *Journal of Advances in Modeling Earth Systems*, **11**, 4513-4558, doi:
588 10.1029/2019MS001739.

589 SHADOZ. 2023. SHADOZ Data Archive [Dataset], https://tropo.gsfc.nasa.gov/shadoz/Archive.html
590 (last accessed 01/06/2022).

591 Sitch, S., Cox, P.M., Collins, W.J., et al. 2007. Indirect radiative forcing of climate change through
592 ozone effects on the land-carbon sink. *Nature*, **448**, 791-794, doi: 10.1038/nature06059.

593 Sofieva, V.F., Tamminen, J., Kyrölä, E., et al. 2014. A novel tropopause-related climatology of ozone
594 profiles. *Atmospheric Chemistry and Physics*, **14**, 283–299, doi:10.5194/acp-14-283-2014.

595 Stevenson, D.S., Young, P.J., Naik, V., et al. 2013. Tropospheric ozone changes, radiative forcing and
596 attribution to emissions in the Atmospheric Chemistry and Climate Model Intercomparison Project
597 (ACCMIP), *Atmospheric Chemistry and Physics*, **13**, 3063- 3085, doi: 10.5194/acp-13-3063-2013.

598 Szopa, S., V. Naik, B. Adhikary, P. Artaxo, T. Berntsen, W.D. Collins, S. Fuzzi, L. Gallardo, A. Kiendler-
599 Scharr, Z. Klimont, H. Liao, N. Unger, and P. Zanis.: Short-Lived Climate Forcers. In Climate Change
600 2021: The Physical Science Basis. Contribution of Working Group I to the Sixth Assessment Report of
601 the Intergovernmental Panel on Climate Change, edited by Masson-Delmotte, V., P. Zhai, A. Pirani,
602 S.L. Connors, C. Péan, S. Berger, N. Caud, Y. Chen, L. Goldfarb, M.I. Gomis, M. Huang, K. Leitzell,
603 E. Lonnoy, J.B.R. Matthews, T.K. Maycock, T. Waterfield, O. Yelekçi, R. Yu, and B. Zhou., Cambridge
604 University Press, Cambridge, United Kingdom and New York, NY, USA, pp. 817–922,
605 doi:10.1017/9781009157896.008, 2021.

606 TOMCAT. 2023. TOMCAT Simulations [Dataset],
607 https://homepages.see.leeds.ac.uk/~earrjpo/to3re/tomcat/ (last accessed 23/01/2023).

608 van der Werf, G. R., Randerson, J. T., Giglio, L., et al. 2017. Global fire emissions estimates during
609 1997–2016. *Earth System Science Data*, **9**, 697–720, doi:10.5194/essd-9-697-2017.

610 Wespes, C., Hurtmans, D., Clerbaux, C., Boynard, A., and Coheur, P.-F.: Decrease in tropospheric O_3
611 levels in the Northern Hemisphere observed by IASI, Atmos. Chem. Phys., 18, 6867–6885,
612 https://doi.org/10.5194/acp-18-6867-2018, 2018.

613 WMO, Meteorology—A three-dimensional science, World Meteorological Organisation, Bulletin 6,
614 (Oct), 134–138, 1957.

615 Worden, H.M., Bowman, K.W., Worden, J.R., et al. 2008. Satellite measurements of the clear-sky
616 greenhouse effect from tropospheric ozone. *Nature Geoscience*, 1, 305-308, doi:
617 doi.org/10.1038/ngeo182.

618 Worden, H.M., Bowman, K.W., Kulawik, S.S., et al. 2011. Sensitivity of outgoing longwave radiative
619 flux to the global vertical distribution of ozone characterized by instantaneous radiative kernels from
620 Aura-TES. *Journal of Geophysical Research: Atmospheres*, 116 (D14115), doi:10.1029/2010JD015101.

621 WOUDC. 2023. Data Search/Download [Dataset], https://woudc.org/data/explore.php (last accessed
622 01/06/2022).

623 Young, P.J., Archibald, A.T., Bowman, K.W., et al. 2013. Pre-industrial to end 21st century projections
624 of tropospheric ozone from the Atmospheric Chemistry and Climate Model Intercomparison Project
625 (ACCMIP). *Atmospheric Chemistry and Physics*, **13**, 2063-2090, doi: 10.5194/acp-13-2063-2013.

626 Ziemke, J.R., Douglass, A.R., Oman, L.D., Strahan, S.E. and Duncan, B.N.: Tropospheric ozone variability
627 in the tropics from ENSO to MJO and shorter timescales. Atmospheric Chemistry and Physics, **15** (14),
628 8037-8049, doi: 10.5194/acp-15-8037-2015, 2015.

629 **Figures and Tables:**

Dataset	TCO_3 (DU)	TO_3RE (W/m^2)	NTO_3RE ($W/m^2/DU$)	TO_3RE Trend (%/yr)	TO_3RE CoV (%)	$DOFS_{trop}$	$DOFS_{utls}$
FORLI	32.6	1.23	37.8	-0.64 (-0.99, -0.28; p = 0.00) -0.21 (-0.66, 0.23; p = 0.35)*	2.5 (1.2)*	1.1	1.2
SOFRID	29.9	1.21	40.4	-0.01 (-0.14, 0.12; p = 0.94)	1.1	0.9	1.0
IMS	29.8	1.21	40.6	-0.13 (-0.36, 0.10; p = 0.25)	1.1	1.2	1.0
TC-CLT	30.7	1.26	41	-0.05 (-0.40, 0.30; p = 0.78)	1.5		
TC-EMS	30.6	1.25	40.8	-0.23 (-0.59, 0.13; p = 0.20)	1.7		
TC-MET	30.1	1.27	41	0.26 (0.13, 0.39; p = 0.00)	0.9		

630 **Table 1:** Summary statistics of the satellite and TOMCAT TCO_3, TO_3RE and NTO_3RE global average
631 (2008-2017) metrics and the corresponding linear trends and covariance of variation (CoV) from
632 **Figures 1-3**. TC-CTL, TC-EMS and TC-MET represent the control, fixed emissions and fixed
633 meteorology runs, respectively. The global average (2008) degrees of freedom of signal (DOFS) for
634 the IASI products are shown for the troposphere (approximately the surface to 200 hPa) and the
635 upper troposphere – lower stratosphere (UTLS – approximately 400-100 hPa). * represents the IASI-
636 FORLI trends for 2011-2017.

637

638

639

640

641
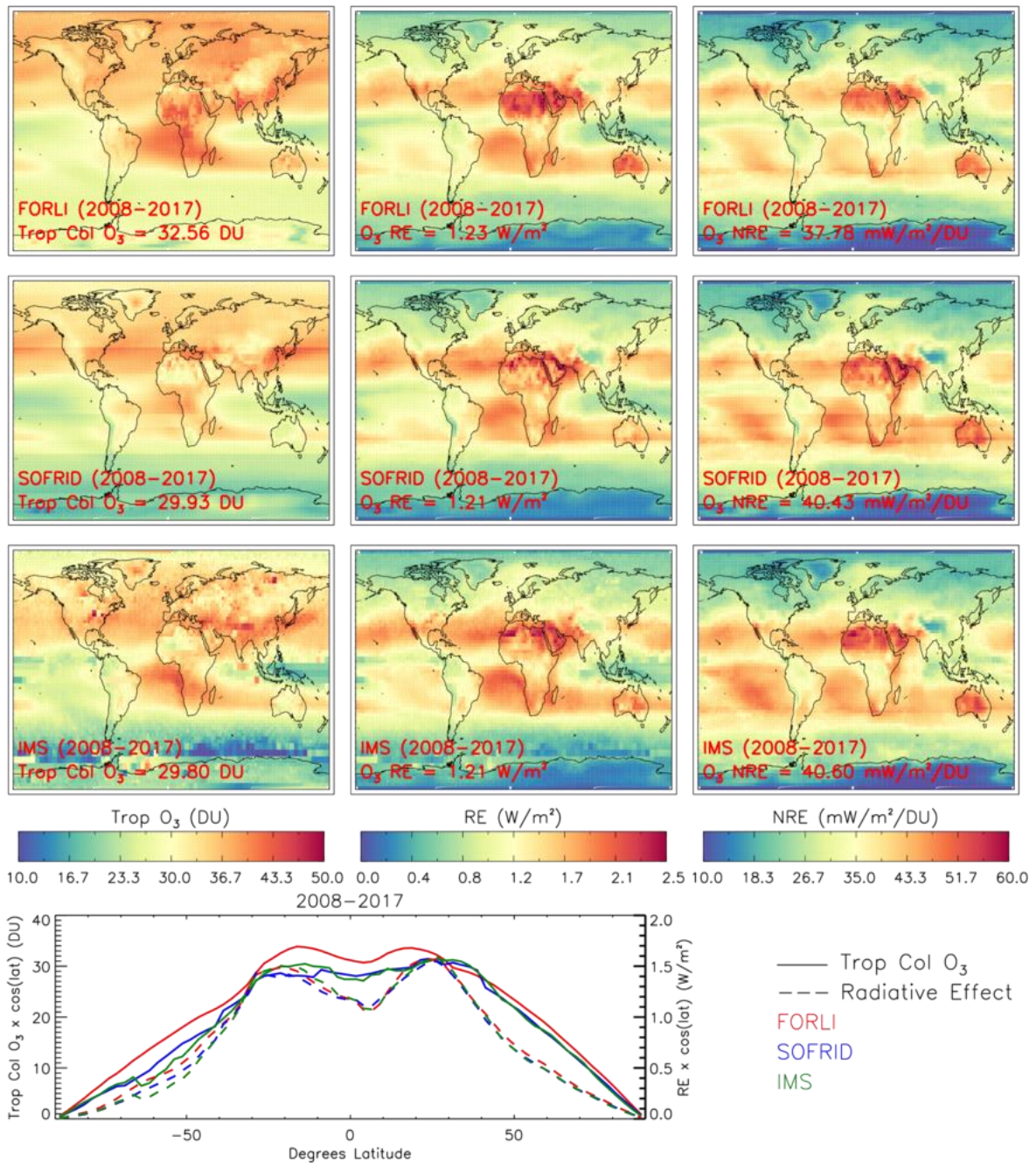
642
Figure 1: *Tropospheric column O_3 (TCO$_3$, DU), tropospheric O_3 radiative effect (TO$_3$RE, W/m^2) and normalised TO$_3$RE (NTO$_3$RE, mW/m^2/DU) averaged for 2008 to 2017 for IASI-FORLI (top row), IASI-SOFRID (middle row) and IASI-IMS (bottom row). Zonal averages of TCO$_3$ (DU, solid lines) and TO$_3$RE (W/m^2, dashed lines), both weighted by cosine of latitude, is shown in the bottom panel from all the IASI instruments.*
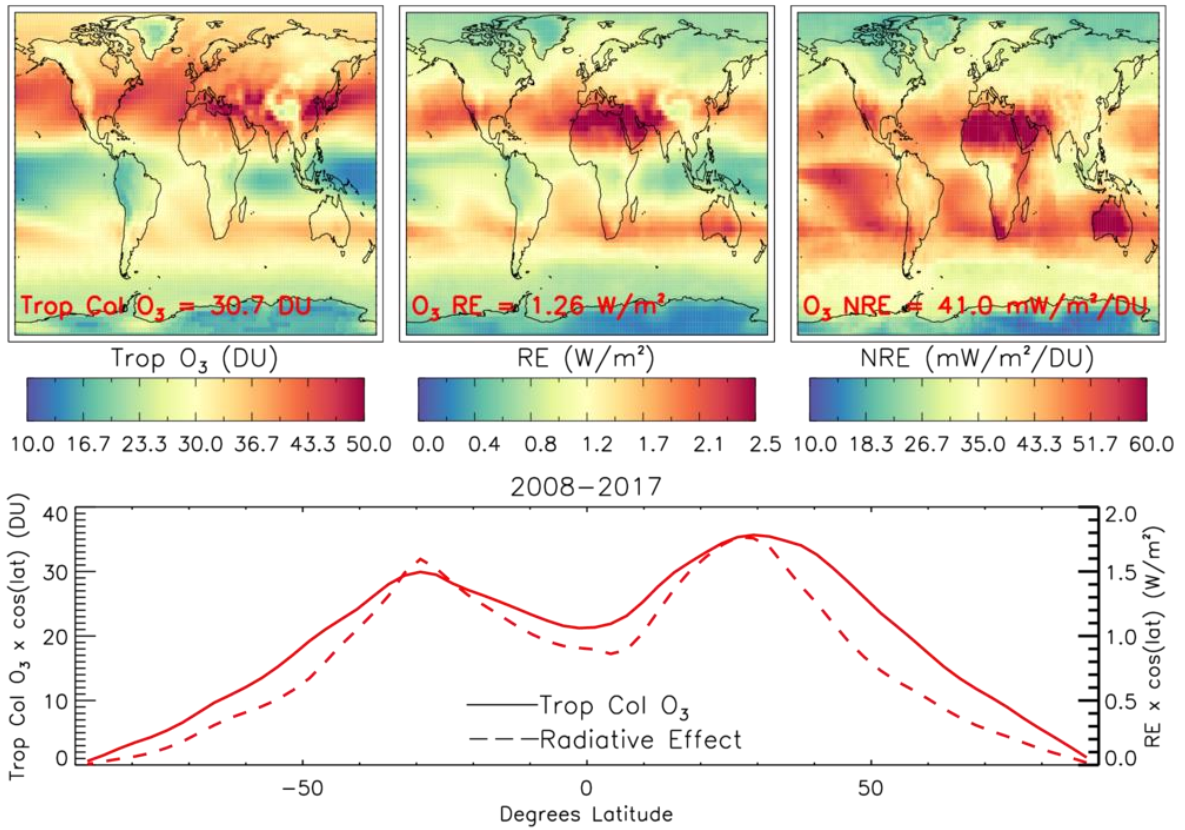
648
649 **Figure 2**: *TCO$_3$ (DU), TO$_3$RE (W/m^2) and NTO$_3$RE (mW/m^2/DU) averaged for 2008 to 2017 for*
650 *TOMCAT. Zonal averages of TCO$_3$ (DU, solid lines) and TO$_3$RE (W/m^2, dashed lines), both weighted by*
651 *cosine of latitude, is shown in the bottom panel from TOMCAT.*

652

653

654

655

656

657
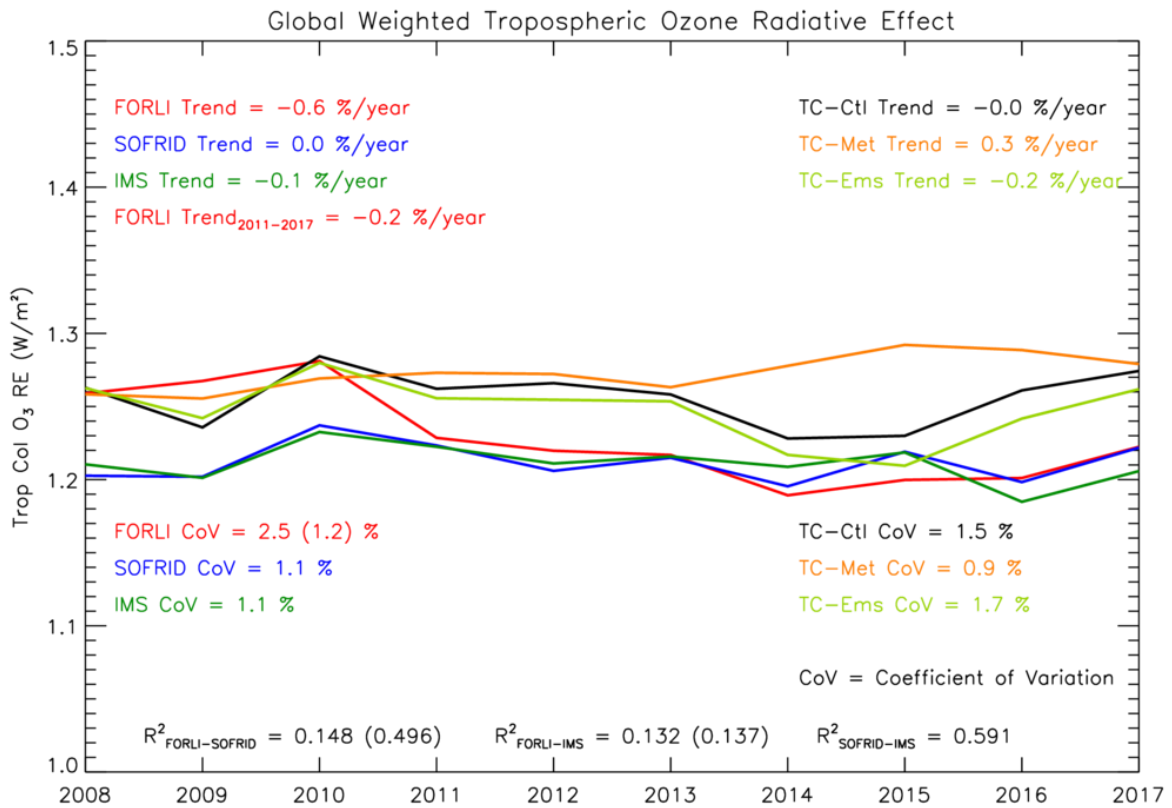
Figure 3: *Annual global mean time-series of TO₃RE (W/m²), between 2008 and 2017, for IASI-FORLI
(red-solid), IASI-SOFRID (blue-solid) and IASI-IMS (green-solid). TOMCAT simulation (black-solid),
TOMCAT with fixed emissions (lime-solid) and TOMCAT with fixed meteorology (orange-solid) are
also shown. The linear trend (%/year) is shown as well as the percentage coefficient of variation
(CoV). The correlation between IASI time-series are shown by the R² values. TC represents TOMCAT.
The IASI-FORLI trend for 2011 to 2017 is also shown as well as the CoV and R² in brackets in addition
to the statistical metrics over the full time period due to record inhomogeneities prior to 2011
(Boynard et al., 2018).*

666

667
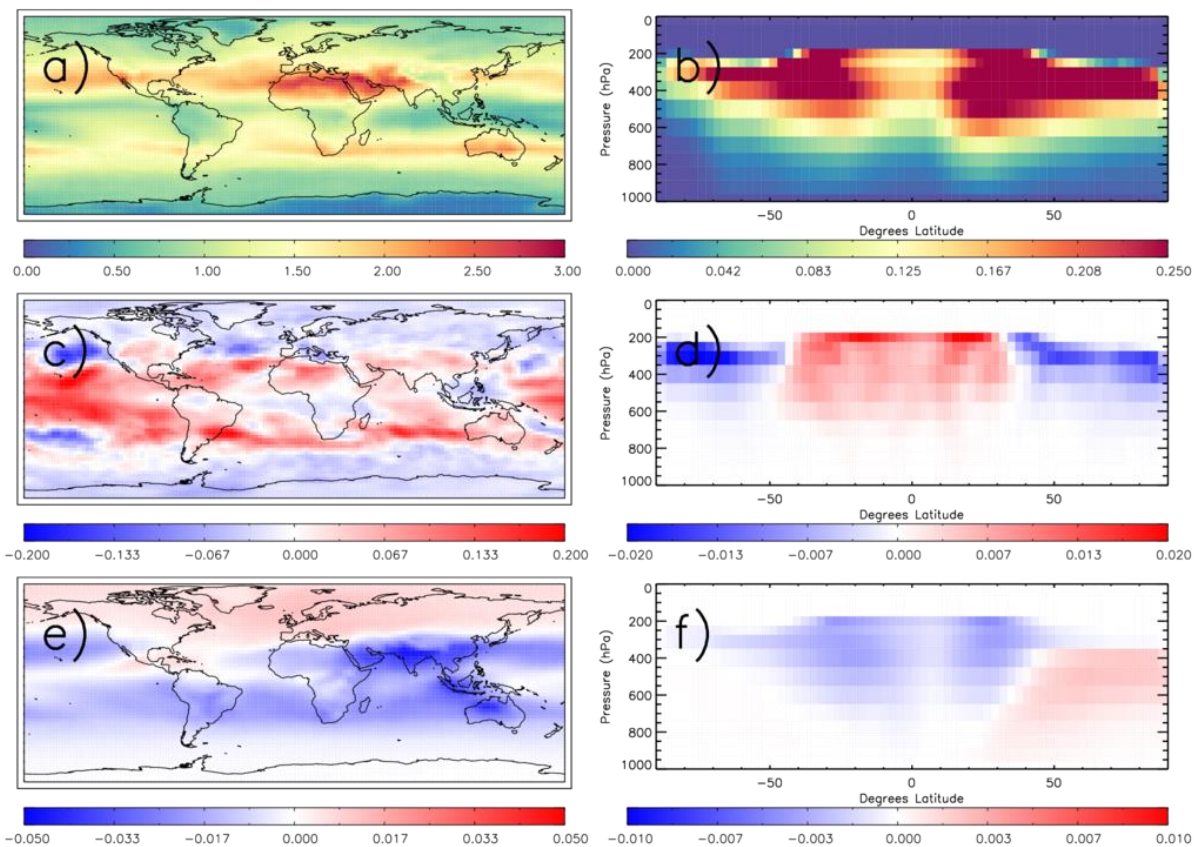
Figure 4: a) *TOMCAT control run TO₃RE (W/m²), b) TOMCAT control run zonal average grid box O₃ radiative effect (W/m²), c) TOMCAT fixed meteorology – TOMCAT control TO₃RE difference (W/m²), d) TOMCAT fixed meteorology – TOMCAT control zonal average grid box O₃ radiative effect difference (W/m²), e) TOMCAT fixed emissions – TOMCAT control TO₃RE difference (W/m²), f) TOMCAT fixed emissions – TOMCAT control zonal average grid box O₃ radiative effect difference (W/m²).*

674